

LETTER

doi:10.1038/nature24298

Spectroscopic identification of r-process nucleosynthesis in a double neutron-star merger

E. Pian, P. D'Avanzo, S. Benetti, M. Branchesi, E. Brocato, S. Campana, E. Cappellaro, S. Covino, V. D'Elia, J. P. U. Fynbo, F. Getman, G. Ghirlanda, G. Ghisellini, A. Grado, G. Greco, J. Hjorth, C. Kouveliotou, A. Levan, L. Limatola, D. Malesani, P. A. Mazzali, A. Melandri, P. Møller, L. Nicastro, E. Palazzi, S. Piranomonte, A. Rossi, O. S. Salafia, J. Selsing, G. Stratta, M. Tanaka, N. R. Tanvir, L. Tomasella, D. Watson, S. Yang, L. Amati, L. A. Antonelli, S. Ascenzi, M. G. Bernardini, M. Boér, F. Bufano, A. Bulgarelli, M. Capaccioli, P. Casella, A. J. Castro-Tirado, E. Chassande-Mottin, R. Ciolfi, C. M. Copperwheat, M. Dadina, G. De Cesare, A. Di Paola, Y. Z. Fan, B. Gendre, G. Giuffrida, A. Giunta, L. K. Hunt, G. L. Israel, Z.-P. Jin, M. M. Kasliwal, S. Klose, M. Lisi, F. Longo, E. Maiorano, M. Mapelli, N. Masetti, L. Nava, B. Patricelli, D. Perley, A. Pescalli, T. Piran, A. Possenti, L. Pulone, M. Razzano, R. Salvaterra, P. Schipani, M. Spera, A. Stamerra, L. Stella, G. Tagliaferri, V. Testa, E. Troja, M. Turatto, S. D. Vergani & D. Vergani

This is a PDF file of a peer-reviewed paper that has been accepted for publication. Although unedited, the content has been subjected to preliminary formatting. *Nature* is providing this early version of the typeset paper as a service to our customers. The text and figures will undergo copyediting and a proof review before the paper is published in its final form. Please note that during the production process errors may be discovered which could affect the content, and all legal disclaimers apply.

Cite this article as: Pian, E. et al. Spectroscopic identification of r-process nucleosynthesis in a double neutron-star merger. *Nature* http://dx.doi.org/10.1038/nature24298 (2017).

Received 12 September; accepted 20 September 2017.
Accelerated Article Preview Published online 16 October 2017.

Spectroscopic identification of r-process nucleosynthesis in a double neutron-star merger

E. Pian¹, P. D'Avanzo², S. Benetti³, M. Branchesi^{4,5}, E. Brocato⁶, S. Campana², E. Cappellaro³, S. Covino², V. D'Elia^{6,7}, J. P. U. Fynbo⁸, F. Getman⁹, G. Ghirlanda², G. Ghisellini², A. Grado⁹, G. Greco^{10,11}, J. Hjorth⁸, C. Kouveliotou¹², A. Levan¹³, L. Limatola⁹, D. Malesani⁸, P. A. Mazzali^{14,15}, A. Melandri², P. Møller¹⁶, L. Nicastro¹, E. Palazzi¹, S. Piranomonte⁶, A. Rossi¹, O. S. Salafia^{2,17}, J. Selsing⁸, G. Stratta^{10,11}, M. Tanaka¹⁸, N. R. Tanvir¹⁹, L. Tomasella³, D. Watson⁸, S. Yang^{20,21}, L. Amati¹, L. A. Antonelli¹⁶, S. Ascenzi^{6,22,23}, M. G. Bernardini^{2,24}, M. Boë²⁵, F. Bufano²⁶, A. Bulgarelli¹, M. Capaccioli^{9,27}, P. Casella⁶, A. J. Castro-Tirado²⁸, E. Chassande-Mottin²⁹, R. Ciolfi^{3,30}, C. M. Copperwheat¹⁴, M. Dadina¹, G. De Cesare¹, A. Di Paola⁶, Y. Z. Fan³¹, B. Gendre³², G. Giuffrida⁶, A. Giunta⁶, L. K. Hunt³³, G. L. Israel⁶, Z.-P. Jin³¹, M. M. Kasliwal³⁴, S. Klose³⁵, M. Lisi⁶, F. Longo³⁶, E. Maiorano¹, M. Mapelli^{3,37}, N. Masetti^{3,38}, L. Nava^{2,39}, B. Patricelli⁴⁰, D. Perley¹⁴, A. Pescalli^{2,41}, T. Piran⁴², A. Possenti⁴³, L. Pulone⁶, M. Razzano⁴⁰, R. Salvaterra⁴⁴, P. Schipani⁹, M. Spera³, A. Stamerra^{40,45}, L. Stella⁶, G. Tagliaferri², V. Testa⁶, E. Troja⁴⁶, M. Turatto³, S. D. Vergani^{2,47} & D. Vergani¹

The merger of two neutron stars is predicted to give rise to three major detectable phenomena: a short burst of γ -rays, a gravitational-wave signal, and a transient optical–near-infrared source powered by the synthesis of large amounts of very heavy elements via rapid neutron capture (the r-process)^{1–3}. The transients, named ‘macronovae’ or ‘kilonovae’^{4–7}, are believed to be cradles of production of rare elements such as gold and platinum⁸. The most compelling evidence so far for a kilonova was a very faint near-infrared rebrightening in the afterglow of a short γ -ray burst^{9,10} at redshift $z=0.356$, although suggestive findings of bluer events have been reported¹¹. Here we report the spectral identification and describe the physical properties of a bright kilonova associated with the gravitational-wave source GW170817 (ref. 12) and γ -ray burst GRB 170817A (refs 13, 14) associated with a galaxy at a distance of 40 megaparsecs. Using a series of spectra from ground-based observatories covering the ultraviolet through the near-infrared wavelength range, we find that the kilonova can be characterized by rapidly expanding ejecta with line features similar to those predicted in current models^{15,16}. The ejecta are optically thick early on, with a velocity of about 0.2 times light speed, reaching a radius of about 50 astronomical units in only 1.5 days. As the ejecta expand, atomic species imprint broad absorption-like lines on the spectral continuum, the products of nucleosynthesis occurring in a post-

merger fast-moving (0.2 times light speed) dynamical ejecta and two slower (0.05 times light speed) wind regions. Comparison with spectral models suggests that the merger ejected 0.03–0.05 solar masses, including high-opacity lanthanides.

GW170817 was detected on 2017 August 17, 12:41:04 UT (ref. 12). A weak, short-duration ($t \approx 2$ s) GRB in the GW error area triggered the Fermi–GBM about two seconds later¹³, and was detected also by the INTEGRAL SPI-ACS (ref. 14; Zhang *et al.*, manuscript in preparation). A significantly improved sky localization was obtained from the joint analysis of LIGO and Virgo data of the GW event, with a 90% error region of 33.6 square degrees (ref. 12). Following this joint GW/GRB detection, a world-wide extensive observational campaign started, using space and ground-based telescopes to scan the sky region where the events were detected. A new point-like optical source, named SSS17a/DLT17ck (coordinates RA(J2000)=13:09:48.09, dec.(J2000)=−23:22:53.3) was rapidly reported (see refs 17, 18), located at 10 arcsec from the center of the S0 galaxy NGC 4993 ($z=0.00968$; ref. 19) in the ESO 508-G018 group at a distance of 40 Mpc, consistent with the luminosity distance of the GW signal.

We carried out targeted and wide field optical/NIR imaging observations of several bright galaxies within the reconstructed sky localization of the GW signal with the Rapid Eye Mount (REM) telescope and with the ESO VLT Survey Telescope (ESO-VST). This led to the detection

¹INAF, Institute of Space Astrophysics and Cosmic Physics, Via Gobetti 101, I-40129 Bologna, Italy. ²INAF, Osservatorio Astronomico di Brera, Via E. Bianchi 46, I-23807 Merate, Italy. ³INAF, Osservatorio Astronomico di Padova, Vicolo dell'Osservatorio 5, I-35122 Padova, Italy. ⁴Gran Sasso Science Institute, Viale F. Crispi 7, L'Aquila, Italy. ⁵INFN, Laboratori Nazionali del Gran Sasso, I-67100 L'Aquila, Italy. ⁶INAF, Osservatorio Astronomico di Roma, Via di Frascati 33, I-00078 Monteporzio Catone, Italy. ⁷Space Science Data Center, ASI, Via del Politecnico, 00133 Roma, Italy. ⁸Dark Cosmology Centre, Niels Bohr Institute, University of Copenhagen, Juliane Maries Vej 30, DK-2100 Copenhagen Ø, Denmark. ⁹INAF, Osservatorio Astronomico di Capodimonte, salita Moiariello 16, I-80131 Napoli, Italy. ¹⁰Università degli Studi di Urbino ‘Carlo Bo’, Dipartimento di Scienze Pure e Applicate, Pza Repubblica 13, I-61029 Urbino, Italy. ¹¹INFN, Sezione di Firenze, I-50019 Sesto Fiorentino, Italy. ¹²Astronomy, Physics, and Statistics Institute of Sciences (APSIS) and Department of Physics, The George Washington University, Corcoran Hall, Washington DC 20052, USA. ¹³Department of Physics, University of Warwick, Gibbet Hill Road, Coventry CV4 7AL, UK. ¹⁴Astrophysics Research Institute, Liverpool John Moores University, Liverpool Science Park, IC2, 146 Brownlow Hill, Liverpool L3 5RF, UK. ¹⁵Max-Planck-Institut für Astrophysik, Karl-Schwarzschild-Strasse 1, 85748 Garching bei München, Germany. ¹⁶European Southern Observatory, Karl-Schwarzschild-Strasse 2, D-85748 Garching bei München, Germany. ¹⁷Dipartimento di Fisica ‘G. Occhialini’, Università degli Studi di Milano-Bicocca, Pza della Scienza 3, I-20126 Milano, Italy. ¹⁸National Astronomical Observatory of Japan, Mitaka, Tokyo, Japan. ¹⁹Department of Physics and Astronomy, University of Leicester, University Road, Leicester LE1 7RH, UK. ²⁰Department of Astronomy and Physics, Padova University, Padova, Italy. ²¹Department of Astronomy, University of California, Davis, California, USA. ²²Dipartimento di Fisica, Università di Roma La Sapienza, P.le A. Moro 2, I-00185 Rome, Italy. ²³Università di Roma Tor Vergata, Via della Ricerca Scientifica 1, I-00133 Roma, Italy. ²⁴Laboratoire Univers et Particules de Montpellier, Université Montpellier 2, 34095 Montpellier, France. ²⁵ARTEMIS (UCA, CNRS, OCA), Boulevard de l'Observatoire, CS 34229, F-06304 Nice Cedex 4, France. ²⁶INAF — Osservatorio Astronomico di Catania, Via S. Sofia 78, I-95123 Catania, Italy. ²⁷Department of Physics, University of Naples Federico II, Corso Umberto I 40, 80138 Napoli, Italy. ²⁸Institute of Astrofísica de Andalucía (CSIC), Glorieta de la Astronomía, E-18008 Granada, Spain. ²⁹APC, Université Paris Diderot, CNRS/IN2P3, CEA/Irfu, Obs de Paris, Sorbonne Paris Cité, France. ³⁰INFN-TIFPA, Trento Institute for Fundamental Physics and Applications, Via Sommarive 14, I-38123 Trento, Italy. ³¹Key Laboratory of Dark Matter and Space Astronomy, Purple Mountain Observatory, Chinese Academy of Science, Nanjing 210008, China. ³²University of Virgin Islands, 2 John Brewer's Bay, St Thomas, Virgin Islands 00802, USA. ³³INAF — Osservatorio Astrofisico di Arcetri, Largo Enrico Fermi 5, I-50125 Florence, Italy. ³⁴Division of Physics, Mathematics and Astronomy, California Institute of Technology, Pasadena, California 91125, USA. ³⁵Thüringer Landessternwarte Tautenburg, Sternwarte 5, D-07778 Tautenburg, Germany. ³⁶University of Trieste and INFN Trieste, I-34127 Trieste, Italy. ³⁷Institute for Astrophysics and Particle Physics, University of Innsbruck, Technikerstrasse 25/8, A-6020 Innsbruck, Austria. ³⁸Departamento de Ciencias Fisicas, Universidad Andrés Bello, Fernández Concha 700, Las Condes, Santiago, Chile. ³⁹INAF, Osservatorio Astronomico di Trieste, Via G.B. Tiepolo 11, I-34143 Trieste, Italy. ⁴⁰Scuola Normale Superiore, Piazza dei Cavalieri 7, I-56126 Pisa, Italy. ⁴¹Università degli Studi dell'Insubria, via Valleggio 11, I-22100 Como, Italy. ⁴²Racah Institute of Physics, The Hebrew University of Jerusalem, Jerusalem 91904, Israel. ⁴³INAF, Osservatorio Astronomico di Cagliari, Via della Scienza 5, I-09047 Selargius, Italy. ⁴⁴INAF, Istituto di Astrofisica Spaziale e Fisica Cosmica di Milano, via E. Bassini 15, I-20133 Milano, Italy. ⁴⁵INAF, Osservatorio Astronomico di Torino, Pino Torinese, Italy. ⁴⁶NASA, Goddard Space Flight Center, Greenbelt, Maryland 20771, USA. ⁴⁷GEPI, Observatoire de Paris, PSL Research University, CNRS, Place Jules Janssen, 92190 Meudon, France.

of SSS17a in the REM images of the field of NGC 4993 obtained 12.8 h after the GW/GRB event. Following the detection of this source, we started an imaging and spectroscopic follow-up campaign at optical and NIR wavelengths. Imaging was carried out with the REM, ESO-VST and ESO-VLT telescopes. A series of spectra was obtained with the VLT/X-shooter, covering the wavelength range 3,200–24,800 Å with VLT/FORS2, covering 3,500–9,000 Å, and with Gemini-S/GMOS covering 5,500–9,000 Å (see ref. 20 for GMOS reduction and analysis details). Overall, we observed the source with an almost daily cadence during the period 2017 August 18 to 2017 September 2 (about 0.5–15.5 days after the GW/GRB trigger; details are provided in Methods). We present here the results of the observations carried out in August 2017.

As described in the following, the analysis and modelling of the spectral characteristics of our dataset, together with their evolution with time, result in a good match with the expectations for kilonovae, providing the first compelling observational evidence for the existence of such elusive transient sources. Details of the observations are provided in the Methods section.

We adopted a foreground Milky-Way extinction of $E(B - V) = 0.1$ mag and the extinction curve of ref. 21, and used this to correct both magnitudes and spectra (see Methods). The extinction within the host galaxy is negligible, based on the absence of significantly detected characteristic narrow absorption features associated with its interstellar medium. The optical light curve resulting from our data is shown in Fig. 1 and the sequence of X-shooter, FORS2, and GMOS spectra in Fig. 2. Apart from Milky Way foreground lines the spectrum is otherwise devoid of narrow features that could indicate association with NGC 4993. In the slit, displaced from the position of the transient from 3''–10'' (0.6–2.0 kpc in projection), we detect narrow emission lines exhibiting significant structure, both spatially and in velocity space (receding at 100–250 km s⁻¹ with respect to the systemic velocity) likely caused by the slit crossing a spiral structure of the galaxy (see Methods).

The first X-shooter spectrum of the transient shows a bright, blue continuum across the entire wavelength coverage—with a maximum at about 6,000 Å and total luminosity of 3.2×10^{41} erg s⁻¹—that can be fit with a black-body of temperature $5,000 \pm 200$ K, and a spherical equivalent radius of approximately 8×10^{14} cm. At a phase of 1.5 days after the GW/GRB trigger, this implies an expansion velocity of the ejected material of about 0.2c. The temperature is considerably lower than that inferred from photometric observations about 20 h earlier (about 8,000 K)²², suggesting rapid cooling. On top of this overall black-body shape are undulations that may represent very broad absorption features similar to those suggested in merger ejecta simulations¹⁶. We refrain from connecting these to expansion velocity as they may be blends of many lines with poorly known properties.

In the second epoch, one day later, where the spectrum only covers the optical range, the maximum has moved to longer wavelengths, indicating a rapid cooling. At the third epoch, when information is again available also at NIR wavelengths, the peak has shifted still to 11,000 Å, and the overall spectral shape is quite different, indicating that the photosphere is receding, the ejecta are becoming increasingly transparent, and more lines become visible. The NIR part of the spectrum evolves in flux and shape much less rapidly. Spectrally broad absorption features are observed ($\Delta\lambda/\lambda \approx 0.1$ –0.2). We exclude that these rapid changes can be compatible with supernova time evolution and are instead consistent with a kilonova (see Methods and Extended Data Fig. 2).

Unlike in the case of supernova absorption lines, the identification of kilonova atomic species is not secure. The neutron-rich environment of the progenitors suggests *r*-process nucleosynthesis as the mechanism responsible for the elemental composition of the ejecta. Lacking line identification, various plausible nuclear reaction networks are considered and included in models of radiative transfer of kilonova spectrum formation. A fraction of the synthesized atoms are radioactive: while decaying they heat the ejecta, which then radiate thermally. All atomic species present in the ejecta with their various

degrees of excitation and ionization absorb the continuum and cause the formation of lines. The models aim at reproducing these lines assuming a total explosion energy, a density profile and an ejecta abundance distribution. In kilonovae it is often envisaged that nucleosynthesis takes place in different regions with different neutron excesses and ejecta velocities, typically a post-merger dynamical ejecta region and a disk-wind region.

Various models predict different components and different synthesized masses. Tanaka et al. (2017) presented three models with different electron/proton fractions Y_e (see Methods). We compare our spectra with a scenario where these three components contribute to the observed spectra (Fig. 3): a lanthanide-rich dynamical ejecta region with a proton fraction in the range $Y_e = 0.1$ –0.4 and a velocity of 0.2c (orange in Fig. 3), and two slow (0.05c) wind regions of which one has $Y_e = 0.25$ and mixed (lanthanide-free and lanthanide-rich) composition (green) and one has $Y_e = 0.30$ and is lanthanide-free (blue). Each of these spectra falls short of the observed luminosity by a factor of about 2, while for other predictions^{5,15} the discrepancy is an order of magnitude. In order to investigate the applicability of the model to the present, more luminous, case we have assumed that the involved ejecta mass is larger. By decreasing the high Y_e (0.3) wind component to 30% of the value in the original model, and increasing both the intermediate Y_e (0.25) wind component and the contribution of the dynamical ejecta nucleosynthesis by a factor of 2 we obtain a satisfactory representation of the first spectrum (Fig. 3).

Although direct rescaling of these models is not in principle correct (for larger masses we can expect that the spectrum of each ejecta could change) we can estimate that the ejected mass was about $(0.03$ – $0.05) M_\odot$, and that the high Y_e wind ejecta (blue line) are significantly suppressed, possibly because of viewing angle away from the GRB or a narrow jet angle or both. It is also suggestive that a wide range of Y_e values are realised in the ejecta, possibly as a function of latitude.

At successive epochs, the same components represent in a less satisfactory way the observed spectral features, which indicates that the set of adopted opacities is not completely adequate, as the cooling of the gas is not properly followed by lines of different ionization states, and that the radioactive input may also not be accurately known.

As a short GRB was detected in association with a GW trigger, we evaluated the expected contribution of its afterglow at the epochs of our observations. Nine days after GW170817 trigger time, an X-ray source was discovered by Chandra at a position consistent with the kilonova, at a flux level of about 4.5×10^{-15} erg cm⁻² s⁻¹ (0.3–8 keV). This source could be delayed X-ray afterglow emission from GRB 170817A, produced by an off-beam jet²³. This may account for the otherwise small probability of having an aligned short GRB jet within such a small volume²⁴. The X-ray emission is compatible with different scenarios: a structured jet with an energy per solid angle decreasing with the angular distance from the axis, viewed at large angles (see, for example, ref. 25), a cocoon accelerated quasi-isotropically at mildly relativistic velocities by the jet^{26,27} or a simple uniform jet observed at large angles. All these scenarios predict an optical afterglow much fainter than the kilonova (see Methods). On the other hand, if we assume that the early (0.45 days) optical flux we measured is afterglow emission, we estimate, at the same epoch, an X-ray flux of more than 10^{-12} erg cm⁻² s⁻¹ and a 6-GHz radio flux density of approximately 10 mJy. These estimates are not consistent with the absence of X-ray and radio detections at the corresponding epochs^{28,29}.

Our long and intensive monitoring and wide wavelength coverage enabled the unambiguous detection of time-dependent kilonova emission and sampled fully its time evolution. This not only confirms the association of the transient with the GW, but, combined with the short GRB detection, also proves beyond doubt that at least a fraction of short duration GRBs are indeed associated with compact star mergers. Furthermore, this first detection provides important insights on the environment of merging NSs. The counterpart's location is only about 2 kpc (projected distance) away from the center of an early-type galaxy.

This is a quite common offset for short GRBs (see, for example, ref. 30) and is consistent with predictions from theoretical models of merging NSs (see, for example, ref. 31). Moreover, the counterpart's location does not appear to coincide with any globular cluster, which suggests a field origin for this NS binary, or a relatively low-velocity ejection from a globular cluster. The nearest possible globular clusters are at more than 2.5'' (corresponding to 500 pc) from the source position³². The formation channel of this event would be best explored with future modeling and simulations. Finally, since this GRB was rather under-energetic (isotropic γ -ray output of $\sim 10^{46}$ erg) and likely off-axis with respect to the line of sight, we conclude that there may be a large number of similar nearby off-axis short bursts that are not followed up at frequencies lower than γ -rays. These are also GW emitter candidates and the present event has demonstrated how the search of the randomly oriented parent population of short GRBs can be made effective via coordinated gravitational interferometry and multi-wavelength observations.

Online Content Methods, along with any additional Extended Data display items and Source Data, are available in the online version of the paper; references unique to these sections appear only in the online paper.

Received 12 September; accepted 20 September 2017.

Published online 16 October 2017.

- Lattimer, J. M., Mackie, F., Ravenhall, D. G. & Schramm, D. N. The decompression of cold neutron star matter. *Astrophys. J.* **213**, 225–233 (1977).
- Eichler, D., Livio, M., Piran, T. & Schramm, D. Nucleosynthesis, neutrino bursts and gamma-rays from coalescing neutron stars. *Nature* **340**, 126–128 (1989).
- Li, L.-X. & Paczyński, B. Transient events from neutron star mergers. *Astrophys. J.* **507**, L59–L62 (1998).
- Kulkarni, S. R. Modelling supernova-like explosions associated with gamma-ray bursts with short durations. Preprint at <https://arxiv.org/abs/astro-ph/0510256> (2005).
- Tanaka, M. & Hotokezaka, K. Radiative transfer simulations of neutron star merger ejecta. *Astrophys. J.* **775**, 113 (2013).
- Rosswog, S. et al. Detectability of compact binary merger macronovae. *Class. Quantum Gravity* **34**, 104001 (2017).
- Wollaeger, R. T. et al. Impact of ejecta morphology and composition on the electromagnetic signatures of neutron star mergers. Preprint at <https://arxiv.org/abs/1705.07084> (2017).
- Metzger, B. D. Kilonovae. *Living Rev. Relativ.* **20**, 3 (2017).
- Tanvir, N. R. et al. A 'kilonova' associated with the short-duration γ -ray burst GRB 130603B. *Nature* **500**, 547–549 (2013).
- Berger, E., Fong, W. & Chornock, R. An r-process kilonova associated with the short-hard GRB 130603B. *Astrophys. J.* **774**, L23 (2013).
- Jin, Z.-P. et al. The macronova in GRB 050709 and the GRB-macronova connection. *Nat. Commun.* **7**, 12898 (2016).
- LIGO Scientific Collaboration and Virgo Collaboration. GW170817: observation of gravitational waves from a binary neutron star inspiral. *Phys. Rev. Lett.* <https://doi.org/10.1103/PhysRevLett.119.161101> (2017).
- Goldstein, A. et al. An ordinary short gamma-ray burst with extraordinary implications: Fermi-GBM detection of GRB 170817A. *Astrophys. J.* **848**, <https://doi.org/10.3847/2041-8213/aa8f41> (2017).
- Savchenko, V. et al. INTEGRAL Detection of the First Prompt Gamma-Ray Signal Coincident with the Gravitational Event GW170817. *Astrophys. J.* **848**, <https://doi.org/10.3847/2041-8213/aa8f94> (2017).
- Kasen, D., Fernández, R. & Metzger, B. D. Kilonova light curves from the disc wind outflows of compact object mergers. *Mon. Not. R. Astron. Soc.* **450**, 1777–1786 (2015).
- Tanaka, M. et al. Properties of kilonovae from dynamical and post-merger ejecta of neutron star mergers. Preprint at <https://arxiv.org/abs/1708.09101> (2017).
- Coulter, D. A. et al. Swope Supernova Survey 2017a (SSS17a), the optical counterpart to a gravitational wave source. *Science* <http://doi.org/10.1126/science.aap9811> (2017).
- Valenti, S. et al. The discovery of the electromagnetic counterpart of GW170817: kilonova AT 2017gfo/DTL17ck. *Astrophys. J.* **848**, <https://doi.org/10.3847/2041-8213/aa8edf> (2017).
- Jones, D. H. et al. The 6dF galaxy survey: final redshift release (DR3) and southern large-scale structures. *Mon. Not. R. Astron. Soc.* **399**, 683–698 (2009).
- Kasliwal, M. M. M. et al. Illuminating gravitational waves: a concordant picture of photons from a neutron star merger. *Science* <http://doi.org/10.1126/science.aap9455> (2017).
- Cardelli, J. A., Clayton, G. C. & Mathis, J. S. The relationship between infrared, optical, and ultraviolet extinction. *Astrophys. J.* **345**, 245–256 (1989).
- Malesani, D. et al. LIGO/Virgo G298048: optical spectral energy distribution of SSS17a. *LVC GCN Circ.* **21577** (2017).

- Troja, E. et al. The X-ray counterpart to the gravitational-wave event GW170817. *Nature* <http://doi.org/10.1038/nature24290> (2017).
- Patricelli, B. et al. Prospects for joint observations of gravitational waves and gamma rays from merging neutron star binaries. *J. Cosmol. Astropart. Phys.* **11**, 56 (2016).
- Salafia, O. S., Ghisellini, G., Pescalli, A., Ghirlanda, G. & Nappo, F. Structure of gamma-ray burst jets: intrinsic versus apparent properties. *Mon. Not. R. Astron. Soc.* **450**, 3549–3558 (2015).
- Lazzati, D. et al. Off-axis prompt X-ray transients from the cocoon of short gamma-ray bursts. Preprint at <https://arxiv.org/abs/1709.01468> (2017).
- Nakar, U. & Piran, T. The observable signatures of GRB cocoons. *Astrophys. J.* **834**, 28 (2016).
- Bannister, K. et al. LIGO/Virgo G298048: ATCA detection of a radio source coincident with NGC 4993. *LVC GCN Circ.* **21559** (2017).
- Evans, P. A. et al. Swift and NuSTAR observations of GW170817: detection of a blue kilonova. *Science* <http://doi.org/10.1126/science.aap9580> (2017).
- Fong, W. & Berger, E. Hubble Space Telescope observations of short gamma-ray burst host galaxies: morphologies, offsets, and local environments. *Astrophys. J.* **708**, 9–25 (2010).
- Belczynski, K. et al. A study of compact object mergers as short gamma-ray burst progenitors. *Astrophys. J.* **648**, 1110–1116 (2006).
- Levan, A. J. et al. The environment of the binary neutron star merger GW170817. *Astrophys. J.* **848**, <https://doi.org/10.3847/2041-8213/aa905f> (2017).

Acknowledgements Work in this paper was based on observations made with ESO Telescopes at the Paranal Observatory under programmes ID 099.D-0382 (PI: E. Pian), 099.D-0622 (PI: P. D'Avanzo), 099.D-0191 (PI: A. Grado) and with the REM telescope at the ESO La Silla Observatory under program ID 35020 (PI: S. Campana). Gemini observatory data were obtained under program GS-2017B-DD-1 (PI L. P. Singer). We thank Gemini Observatory for rapidly executing these observations. We thank the ESO Director General for allocating Discretionary Time to this program and the ESO operation staff for excellent support of this program. We acknowledge INAF for supporting the project 'Gravitational Wave Astronomy with the first detections of adLIGO and adVIRGO experiments - GRAWITA' PI: E. Brocato. We acknowledge support from the ASI grant I/004/11/3. J. Hjorth was supported by a VILLUM FONDEN Investigator grant (project number 16599). MMK acknowledges support from the GROWTH (Global Relay of Observatories Watching Transients Happen) project funded by the National Science Foundation under PIRE grant number 1545949.

Author Contributions E. Pian and P. D'Avanzo are Principal Investigators of the two active ESO VLT programmes and coordinated the work. J. Selsing reduced all the X-shooter spectra presented in Fig. 2 and wrote the relevant sections. M. Tanaka developed the kilonova spectral models. E. Cappellaro assisted with the spectral analysis. P. Mazzali provided the liaison between spectral observations and kilonova theory: he coordinated the theoretical interpretation, developed the match between the synthetic and observed spectra (Fig. 3), and wrote the part on their description and discussion. S. Campana coordinated the REM observations. S. Covino, A. Grado and A. Melandri reduced and analysed the optical photometry (Fig. 1). M. M. Kasliwal provided the Gemini spectrum. D. Malesani assisted with early observation planning. G. Ghirlanda, G. Ghisellini and O. S. Salafia wrote the section on the off-beam jet with contributions from L. Amati, Y. Z. Fan, Z. P. Jin and T. Piran. D. Watson assisted with the analysis of spectra in light of thermal models and assisted with paper writing. E. Brocato was the Principal Investigator of the GRAVitational Wave Inaf TeAm (GRAWITA) for GW electromagnetic follow-up. M. Branchesi liaised GRAWITA with LIGO-VIRGO collaborations activities. A. Grado coordinated the ESO-VST observations. L. Limatola and F. Getman developed the pipeline to reduce the VST data. N. Tanvir and A. Levan assisted with NIR data calibration issues. J. P. U. Fynbo, J. Hjorth and C. Kouveliotou assisted with paper writing and short GRB expertise. L. Nicastro supervised the data flow and handling. S. Piranomonte and V. D'Elia contributed to the data reduction and analysis of the X-shooter spectra. E. Palazzi, A. Rossi, G. Stratta and G. Greco participated in the organization of the observations and image analysis and provided specific input for photometry calibration. L. Tomasella, S. Yang, and S. Benetti contributed to the data analysis, with particular reference to ISM spectral features. P. Møller assisted with issues related to ESO policies and observation planning. This effort was led by GRAWITA, that includes most co-authors, and is based on GW electromagnetic follow-up programs at ESO and at many telescopes both in Italy and at the Canary Islands. All GRAWITA members contributed to the work development at many phases from preparation of proposals, coordination with the LIGO-VIRGO collaborations, activation of approved programs at many facilities, data acquisition, reduction, analysis, interpretation and presentation.

Author Information Reprints and permissions information is available at www.nature.com/reprints. The authors declare no competing financial interests. Readers are welcome to comment on the online version of the paper. Publisher's note: Springer Nature remains neutral with regard to jurisdictional claims in published maps and institutional affiliations. Correspondence and requests for materials should be addressed to E.P. (pian@iasfbo.inaf.it).

Reviewer Information *Nature* thanks R. Chevalier, C. Miller and the other anonymous reviewer(s) for their contribution to the peer review of this work.

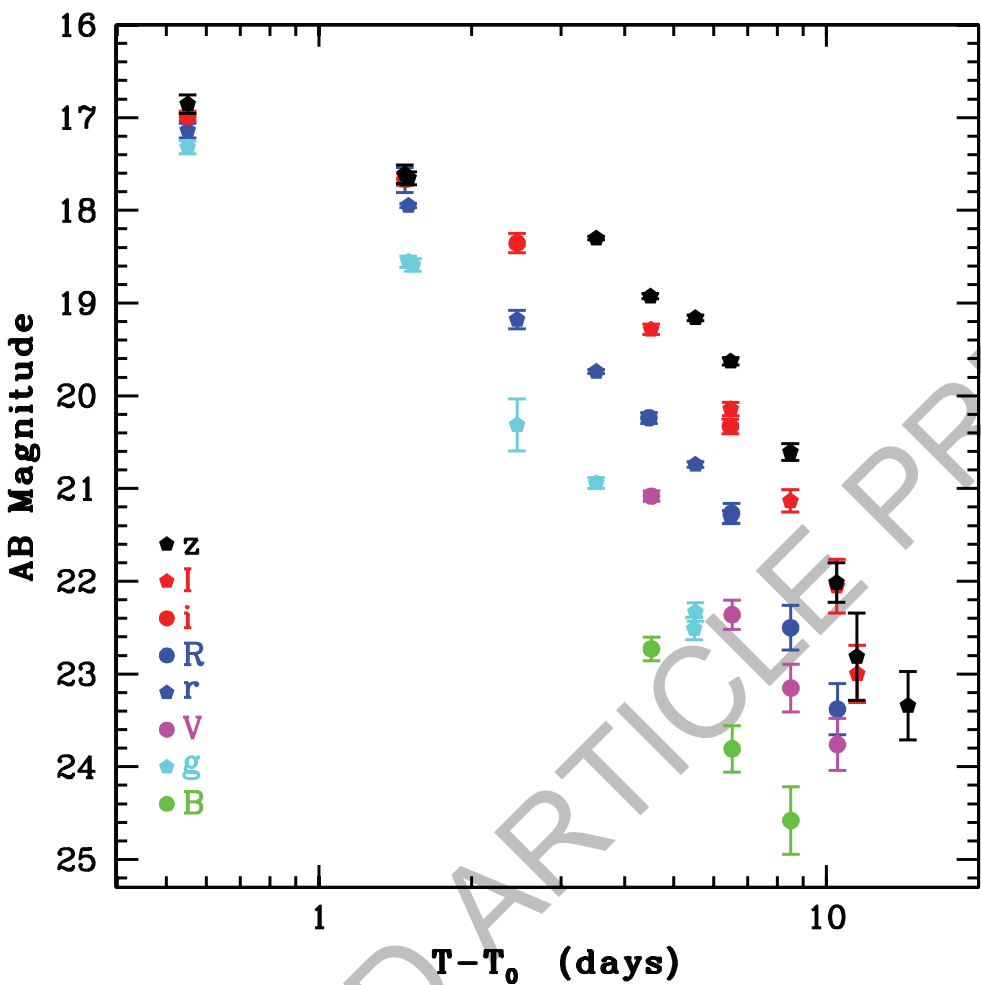


Figure 1 | Multiband optical light curve of SSS17a/DLT17ck. The data reported in Extended Data Table 1 are shown (filled symbols). The data were not corrected for Galactic reddening.

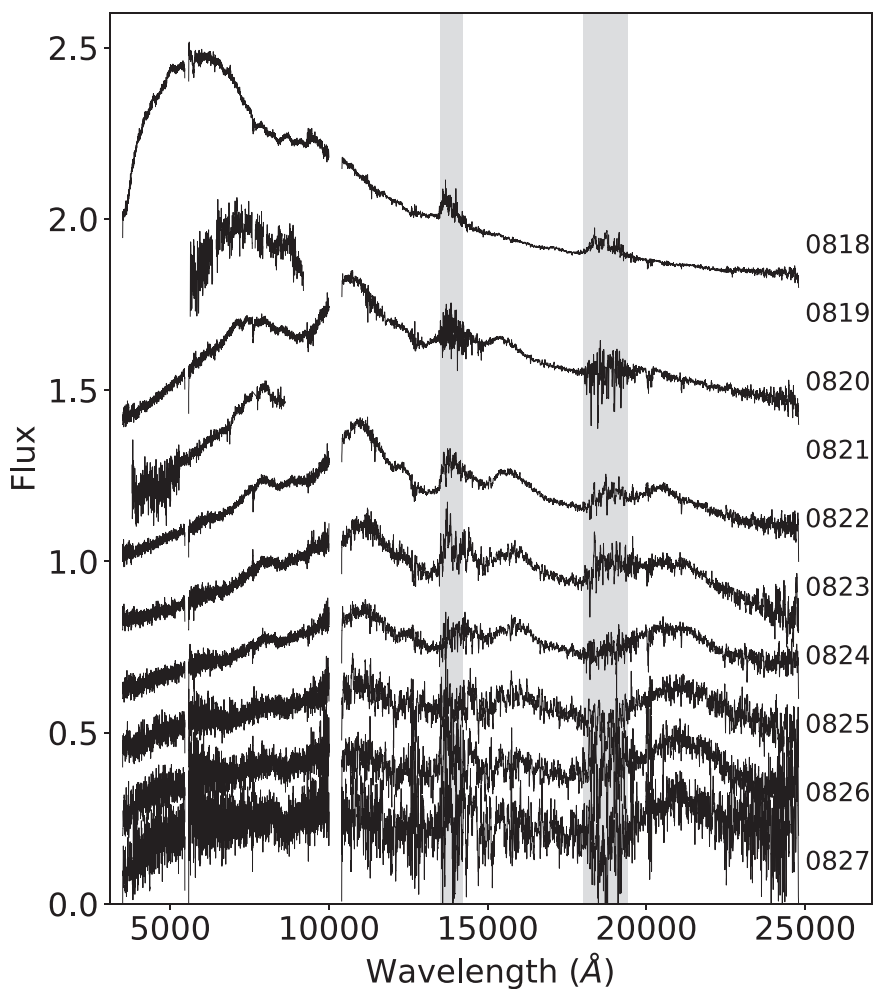


Figure 2 | Time evolution of the SSS17a/DLT17ck spectra. VLT X-shooter, FORS2, and GMOS spectra (phases with respect to explosion are as in Extended Data Table 2; the flux normalization is arbitrary). Spikes and spurious features were removed and a filter median of 21 pixels was applied. The data were not corrected for Galactic reddening.

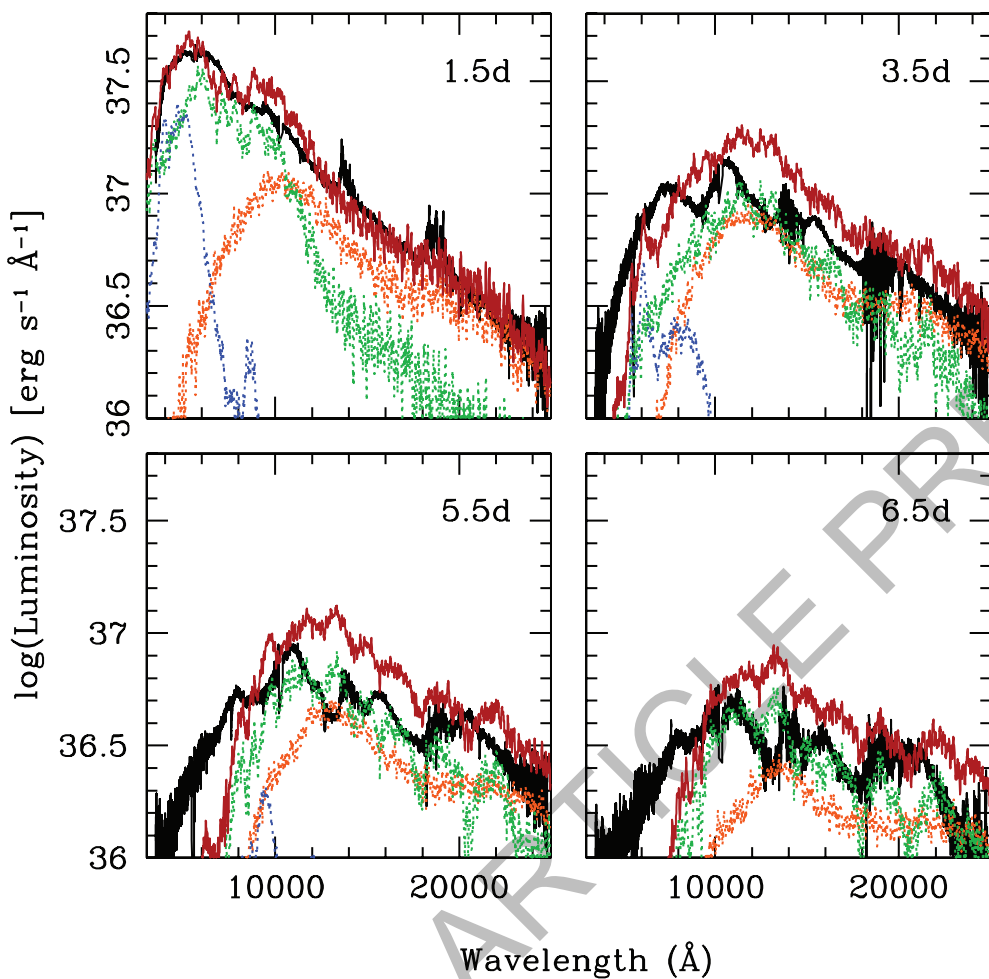


Figure 3 | Kilonova model compared to the SSS17a/DLT17ck spectra. X-shooter spectra at the first four epochs and kilonova models overlaid: dynamical ejecta ($Y_e = 0.1\text{--}0.4$, orange), wind region with $Y_e = 0.3$ (blue) and $Y_e = 0.25$ (green). The burgundy curve represents the sum of the three model components.

METHODS

Optical/NIR imaging. Our first observations of the field of SSS17a were carried out with the 60-cm robotic telescope REM³³ located at the ESO La Silla Observatory (Chile) in the g, r, i, z and H bands starting on 2017 August 18 at 01:29:28 UT (12.8 h after the GW event). The field was included in the selection we made to carry out targeted observations of catalogued galaxies in the LVC skymap aimed at searching for an optical/NIR counterpart of the GW event starting on 2017 August 17 at 23:11:29 UT (10.5 h after the GW event)^{34,35}. Following this first detection, we started an extensive follow-up campaign of optical/NIR imaging carried out with an almost daily cadence from about 1.5–15.5 days after the time of the GW trigger. These observations were performed using the ESO VLT telescopes equipped with the X-shooter acquisition camera, the FORS2 instrument, and the ESO VST equipped with OmegaCam instrument^{36–39}. The complete log of our photometric observations is reported in Extended Data Table 1. The optical/NIR light curves are shown in Fig. 1. Concerning REM and FORS2 imaging, data reduction was carried out following the standard procedures: subtraction of an averaged bias frame and division by a normalized flat frame. The astrometric solution was computed against the USNO-B1.0 catalogue (<http://www.nofs.navy.mil/data/fchpix/>). Aperture photometry was performed using SExtractor⁴⁰ and the PHOTOM package part of the Starlink software distribution (<http://starlink.eao.hawaii.edu/starlink>). The photometric calibration was achieved by observing Landolt standard fields and the Pan-STARRS catalogue (<https://panstarrs.stsci.edu>). In order to minimize any systematic effect, we performed differential photometry with respect to a selection of local isolated and non-saturated reference stars. As shown in Extended Data Fig. 1, the transient is embedded in the host galaxy light, so that the background around the transient position is highly inhomogeneous, making accurate photometry measurements arduous. In order to minimize the effect of flux contamination from the host light, we fitted it with an analytical profile. The result obtained from the fit was then subtracted from the image in a neighborhood of the transient. This procedure was repeated for each frame. After this subtraction, the background around the transient position is much more uniform, enabling accurate photometric measurements. A dedicated procedure was applied for the reduction and analysis of the wide-field images obtained with the VLT Survey Telescope (VST⁴¹). The telescope is equipped with OmegaCam⁴², a camera with one square degree field of view (FOV) matched by 0.21 arcsec pixels scale. Data have been processed with a dedicated pipeline for the VST-OmegaCAM observations (dubbed VST-tube⁴³). The pipeline searches for new data in the ESO Data archive and, if available, automatically downloads and processes them performing the following main steps: pre-reduction; astrometric and photometric calibration; mosaic production. The OT magnitude, in the AB system, is the PSF fitting magnitude measured on the image after subtracting a model of the galaxy obtained fitting the isophotes with the IRAF/STSDAS task ELLIPSE⁴⁴. The reference catalog used for the absolute photometric calibration is the APASS DR9.

FORS2 spectroscopic observations. FORS2 spectra were acquired with the 600B and 600RI grisms, covering altogether the 3,500–8,600 Å wavelength range. We used in all cases a 1'' slit, for an effective resolution of $R \approx 800$ –1,000. Spectral extraction was performed with the IRAF software package (IRAF is the Image Reduction and Analysis Facility made available to the astronomical community by the National Optical Astronomy Observatories, which are operated by AURA, Inc., under contract with the US National Science Foundation; <http://iraf.noao.edu>). Wavelength and flux calibration of the spectra were accomplished using helium–argon lamps and spectrophotometric stars. A check for slit losses was carried out by matching the flux-calibrated spectra to our simultaneous photometry (see Extended Data Tables 1 and 2). This shows that the derived spectral shape is robust.

X-shooter spectroscopic observations. The cross-dispersed echelle spectrograph, X-shooter⁴⁵, mounted on the VLT, was used to observe the optical/near-infrared counterpart of GW170818. The observing campaign started on the night following the discovery and continued until the source had faded below the detection limit (see Extended Data Table 2) of X-shooter. The observations were carried out using a standard ABBA nodding pattern. Similar position angles of the slit were used for all observations. The position of the slit on the source is shown in Extended Data Fig. 1.

The spectroscopic data obtained with X-shooter were managed with the Reflex interface⁴⁶ and reduced using version 2.9.3 of the X-shooter pipeline⁴⁷. The reduction cascade consists of bias subtraction, order tracing, flat fielding, wavelength calibration, flux calibration using the spectrophotometric standard EG274⁴⁸, background subtraction and order rectification—all carried out using the nightly obtained calibration files. A refinement to the wavelength solution was obtained by cross correlating the observed sky spectra with a synthetic sky spectrum^{49,50}, leading to a wavelength solution more accurate than 1 km s⁻¹. Because X-shooter is a cross-dispersed echelle spectrograph, the individual echelle orders are curved across each detector and a rectification algorithm, which correlates neighboring

pixels, must be employed. A sampling of 0.2/0.2/0.6 Å per pixel (in the UVB, VIS, and NIR arms, respectively) in the rectified image was chosen to minimize this correlation while conserving the maximal resolving power. The effective resolving power, R , of each observation was obtained from fits to unsaturated telluric absorption lines and yielded mean values of 4290/8150/5750 in the UVB/VIS/NIR arms, respectively. This is better than nominal values, owing to a seeing PSF being narrower than the slit width. Immediately following the observations each night, telluric standard stars were observed at an airmass comparable to the target from which the atmospheric transmission spectrum was obtained using Molecfit^{51,52}. Host continuum contamination is visible as a faint background gradient along the slit. An effort has been made to minimize this contamination by using the background regions closest to the target. The images are combined in nightly sets using a weighting scheme based on a moving background variance measure wide enough to avoid it being pixel based and therefore unsuitable for Poisson-noise dominated images. For a subset of the observations, the signal-to-noise in the spectral trace is large enough to build a model of the spectral line-spread function to employ an optimal extraction algorithm⁵³, but for the majority of the data, an aperture covering the entire trace is used. To establish an accurate flux calibration, slit loss corrections were calculated using the average seeing FWHM of the nightly observations along with the theoretical wavelength dependence of seeing⁵⁴. The slit losses are obtained by integrating a synthetic 2D PSF over the width of the slits and corrections are made accordingly.

Foreground dust extinction. We have estimated the intervening dust extinction toward the source using the Na I D line doublet at 5,896 Å. On the basis of the strength of the line in our Galaxy we derive $E(B - V) = 0.09$ mag using component D1, $E(B - V) = 0.05$ mag using component D2, and $E(B - V) = 0.06$ mag using the sum⁵⁵. The Galactic extinction is thus limited to $E(B - V) < 0.1$ mag. Similar upper limits on $E(B - V)$ are obtained from the upper limits on the equivalent widths of the undetected K I 7,699 Å absorption line⁵⁶ ($\text{EW} < 0.025$ Å) and undetected 8,620 Å diffuse interstellar band⁵⁷ ($\text{EW} < 0.04$ Å). These estimates and limits are marginally consistent with the value of $E(B - V) = 0.11$ mag obtained from COBE/DIRBE maps covering that sky region⁵⁸.

Spectrum analysis and interpretation. The first epoch X-shooter spectrum was fit with a black-body with temperature of $5,000 \pm 200$ K. The main deviations from this fit are two absorption-like lines at 8,100 Å and 12,300 Å, that evolve with time and become more pronounced in the second spectrum. Altogether, all deviations from a black-body in the first spectrum are below about 10% from 3,500 Å to 20,000 Å, indicating that the fit is very satisfactory. Moreover, the expansion speed of 0.2c we derive from the black-body radius at the epoch of the first spectrum (1.5 days) is compatible with the width of the absorption lines we observe in the second spectrum ($\Delta\lambda/\lambda \approx 0.1$ –0.2), confirming that the black-body emission in the first spectrum is highly efficient.

The first four X-shooter spectra were compared with kilonova models from Tanaka et al. (2017). The model uses atomic structure calculations for Se ($Z=34$), Ru ($Z=44$), Te ($Z=52$), Ba ($Z=56$), Nd ($Z=60$), and Er ($Z=68$) to construct the atomic data for a wide range of r-process elements. By using two different atomic codes, they confirmed that the atomic structure calculations returned uncertainties in the opacities by a factor of up to about 2. Thereafter, they apply multiwavelength radiative transfer simulations to predict a possible variety of kilonova emission. For each model, the abundance is assumed to be homogeneous in the ejecta. However, a high- Y_e component should preferentially dominate near the polar region and low- Y_e /dynamical component develops in the equatorial region. For each model, the energy release is similar to a power-law ($t^{-1.3}$) owing to the sum of the radioactive decays of various nuclei with different lifetimes. The efficiency of the energy deposition is also taken into account, and the energy deposition rate is somewhat steeper than $t^{-1.3}$ because the γ -rays can escape without depositing energy.

We emphasize that we have not attempted a real fit of this model to our X-shooter spectra, but have rather looked into an interpretation that was in reasonable agreement. The match is satisfactory only for the first X-shooter spectrum, and not completely satisfactory for the following three. For this reason, we refrained from deriving a light curve model. Infact, in principle, one may fold the synthetic spectral model with the sensitivity curve of any given broadband filter and integrate the flux in the corresponding band to compare with the observed one. However, the result may be misleading independent of how persuasive it is at face value. The spectral comparison allows one to appreciate in which wavelength ranges the model is effective and in which ones it fails. Integration of the model over a broad wavelength interval cancels the spectral “memory” and prevents a critical judgment. In other words, since the spectral model is not completely satisfactory, the comparison of synthetic and observed photometry is not significant, although it may appear good.

Description of the spectral evolution. The first X-shooter spectrum obtained at $t = 1.5$ d after the GW trigger shows an almost featureless, moderately blue continuum. The overall spectral energy distribution is similar to that of early, broad

line core collapse supernovae. While in general at this relatively low temperature (about 5,000 K) supernovae typically show strong broad features using the supernova spectral classification tool GELATO⁵⁹ a good match is obtained with the early spectra of the type Ib SN2008D/XRF080109⁶⁰. As shown in Extended Data Fig. 2, the X-shooter extended spectral range displays, by comparison with the black-body fit (dotted line) the presence of some large scale modulations that are suggestive of multi-component contributions already suggestive of a kilonova event.

In the next two days the spectrum shows a very rapid evolution. The continuum temperature rapidly drops to about 3,300 K and broad features emerges, with peaks at 10,700 Å and 16,000 Å. The broad features point to very high expansion velocity and the rapid evolution to a low ejected mass. The combined spectral properties and evolution are unlike those of any known supernova types and instead they are very similar to the predicted outcomes of kilonova models.

In the following week the temperature derived from the optical continuum seems to remain roughly constant while the peak at 10,700 Å drifts to longer wavelengths (11,200 Å at day 6) and decreases in intensity until, at ten days from discovery, the dominant feature in the spectrum is a broad emission centered at about 21,000 Å.

Host emission analysis. Extending 3''–10'' (0.6–2.0 kpc in projection) from the position of the GW counterpart are emission lines formed in the host. The lines are identified as [O II]λ3,726, 3,729, Hβ, [O III]λ4,959, 5,007, Hα, [N II]λ6,549, 6,583 and [S II]λ6,717, 6,731, and they exhibit both spatial and velocity structure along the extent of the slit, as shown in Extended Data Fig. 3.

From the brightest blob of emission, centered at 6'' (1.2 kpc in projection) from the source, we measure a receding velocity of $247 \pm 15 \text{ km s}^{-1}$ relative to the host nucleus (adopting a systemic velocity of NGC 4993 of $2,916 \pm 15 \text{ km s}^{-1}$). Along the spatial direction of the slit, closer to the source, the emission line centroids become more blue-shifted, approaching a recession velocity of 100 km s^{-1} relative to the NGC 4993 systemic velocity. The velocity range (150 km s^{-1}) of the line emission along the slit indicates coherent motion of the gas along the slit. This is further supported by the dust lanes visible superposed on the host nucleus, see Extended Data Fig. 1, which extends outwards and curls clockwise around the nucleus and intersects the slit at the position of the line emission. This means that NGC 4993 either has trailing spiral arms and is rotating counter-clockwise or leading spiral arms and rotating clock-wise. The presence of spiral arms was also noted by⁶¹. A strong [N II]λ6,583 relative to Hα combined with a weak Hβ relative to [O III]λ5,007 indicates a radiation field dominated by AGN activity, as also reported previously^{20,62,63} and supported by the presence of a central radio source⁶⁴. Using the Balmer decrement, the inferred extinction at the position of the line emission is $E(B - V) = 0.21 \pm 0.21$.

Off-beam jet scenario. GRB 170817A had a fluence of $2.2 \times 10^{-7} \text{ erg cm}^{-2}$ in the 10–1,000 keV energy range as observed by the GBM which, at a distance of 40 Mpc, corresponds to a γ-ray isotropic equivalent energy $E_{\text{iso}} \approx 4.3 \times 10^{46} \text{ erg}$. The peak energy is $E_{\text{peak}} = 128 \pm 48 \text{ keV}$ (refs 13, 65). The observed E_{iso} is three to four orders of magnitude smaller than the average energy of short GRBs with known redshift^{66,67}.

For illustration let us consider a very simple model: a uniform conical jet of semi-aperture angle θ_{jet} observed off-beam, that is, at a viewing angle $\theta_{\text{view}} > \theta_{\text{jet}}$. In this case larger bulk Lorentz factors Γ correspond to larger de-beaming factors $b = E_{\text{iso}}(0^\circ)/E_{\text{iso}}(\theta_{\text{view}})$ for a fixed θ_{view} (refs 68, 69). Given the small distance of 40 Mpc, and a likely luminosity function decreasing with increasing luminosity (see, for example, refs 70, 71), we can assume that the on-axis luminosity of this burst belongs to the low-luminosity tail. For this reason we assume $E_{\text{iso}}(0^\circ) = 10^{50} \text{ erg}$. Therefore $b = 2,500$. The probability of a jet oriented at an angle less than θ_{view} is $P(<\theta_{\text{view}}) = 1 - \cos(\theta_{\text{view}})$. A probability of at least $P > 10\%$ implies $\theta_{\text{view}} > 26^\circ$. An off-axis viewing angle larger than about 30° is also suggested by the expected rate of joint GW and Fermi-GBM detection²⁴ rescaled to the actual observations. Combining equations (2) and (3) from ref. 68 it is possible to estimate the observed energy E_{iso} and peak energy E_{peak} as a function of θ_{view} and Γ for a given θ_{jet} . With $\theta_{\text{view}} = 30^\circ$, $b = 2,500$ ($E_{\text{iso}}(0^\circ) = 10^{50} \text{ erg}$) requires $\Gamma = 10$ for $\theta_{\text{jet}} = 10^\circ$. The latter is within the currently few estimates of short GRB opening angles⁷² and $\Gamma \approx 10$ is within the dispersion of the Γ - E_{iso} relation^{73,74} for $E_{\text{iso}}(0^\circ) \approx 10^{50} \text{ erg}$. With these values $E_{\text{peak}}(0^\circ)$ turns out to be approximately 2 MeV. The corresponding comoving frame peak energy would be about 100 keV. If photons with much larger energies are absorbed by pair production we should expect (as observed at 30°) a spectral cutoff at about 650 keV which is larger than the observed peak energy reported by the GBM. Though these values of $E_{\text{peak}}(0^\circ)$ and $E_{\text{iso}}(0^\circ)$ are consistent with those observed in short GRBs, they locate this burst relatively far from the possible spectral-energy correlations of short GRBs.

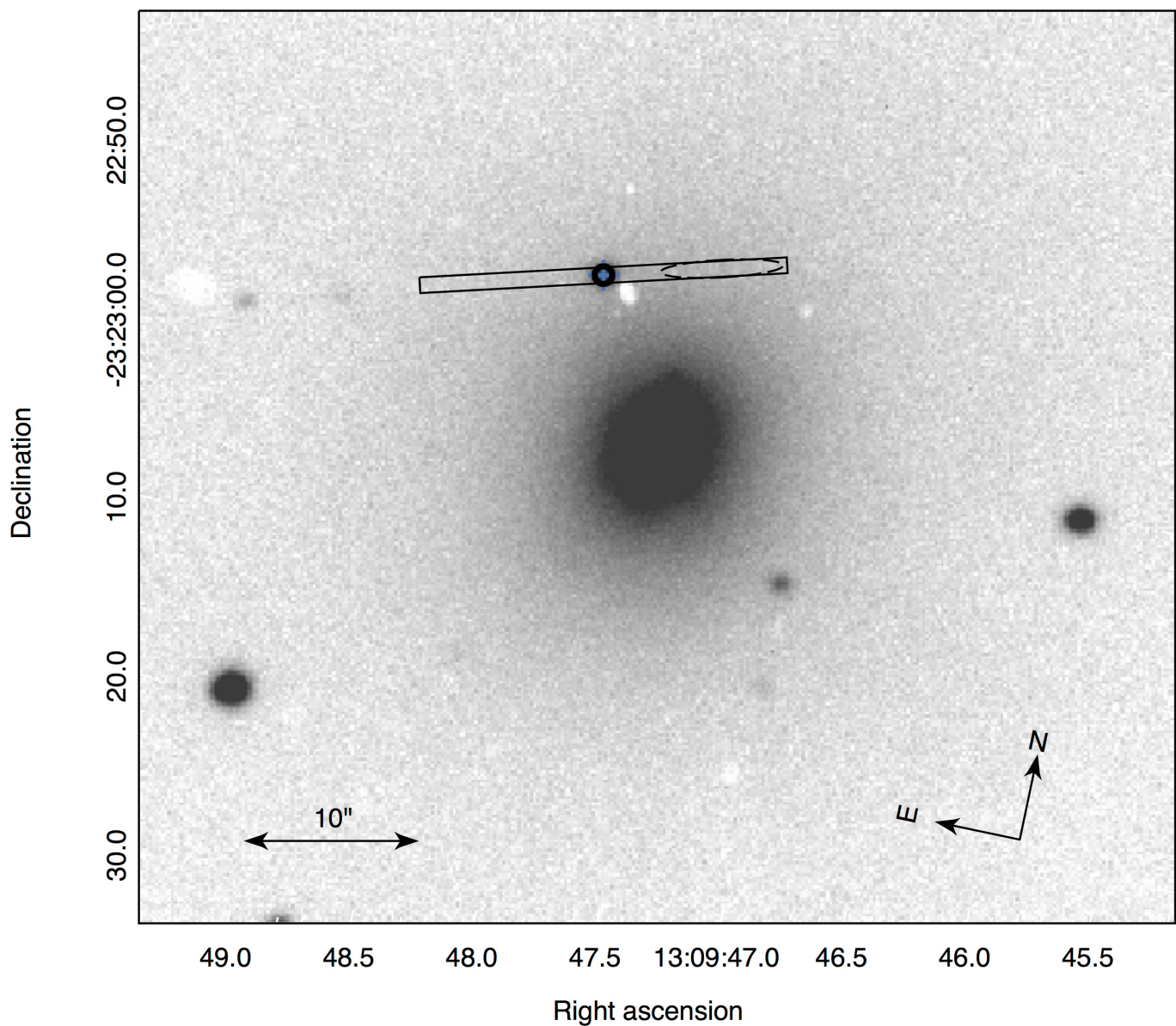
Extended Data Fig. 4 shows the predicted afterglow light curves at 6 GHz (red), R band (green) and 1 keV (blue). The cyan symbol shows the X-ray flux at 15 days (refs 23, 75). The orange arrows show two representative radio upper limits: at 8.65 days (obtained⁷⁶ by co-adding six e-MERLIN observations at 5 GHz)

and at 20 days (obtained⁷⁷ with MeerKAT at 1.5 GHz). For the model curves the assumed parameters are: $\theta_{\text{jet}} = 10^\circ$, $\theta_{\text{view}} = 30^\circ$, isotropic equivalent kinetic energy $E_{\text{kin}} = 10^{50} \text{ erg}$, $\Gamma = 10$, a uniform density ISM with $n = 2 \times 10^{-3} \text{ cm}^{-3}$ and standard micro-physical parameters at the shock, that is, $\varepsilon_e = 0.1$, $\varepsilon_B = 0.01$ and electrons' energy injection power law index $p = 2.1$. Standard afterglow dynamics and radiation codes⁷⁸ are used. As can be seen the R flux is always below $2 \times 10^{-5} \text{ mJy}$, corresponding to $R > 28$, and therefore orders of magnitude lower than the kilonova emission.

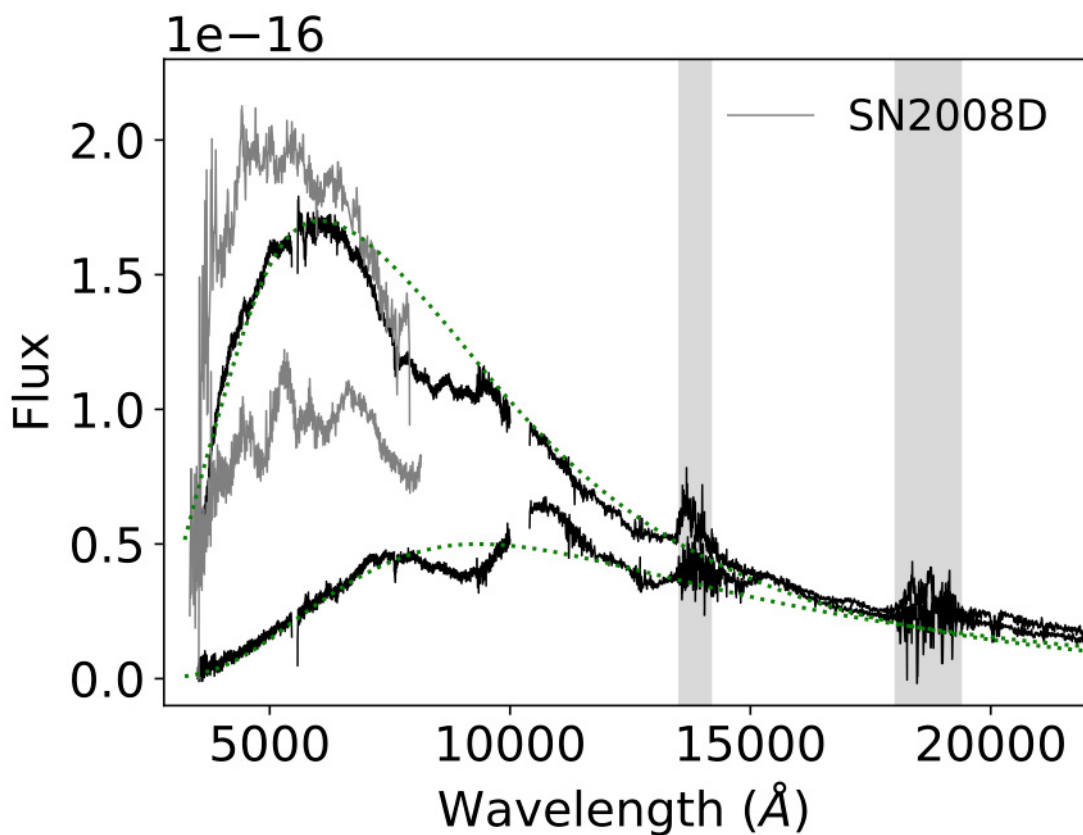
Data availability. The data presented in this paper and supporting the findings of this study are available from the corresponding author upon reasonable request.

33. Chincarini, G. et al. The last born at La Silla: REM, the Rapid Eye Mount. *Messenger* **113**, 40–44 (2003).
34. Melandri, A. et al. LIGO/Virgo G298048: REM optical/NIR observations of candidate in NGC 4993. *LVC GCN Circ.* 21532 (2017).
35. Melandri, A. et al. LIGO/Virgo G298048: REM optical/NIR observations. *LVC GCN Circ.* 21556 (2017).
36. Pian, E. et al. LIGO/Virgo G298048: GRAWITA VLT/X-shooter observations and tentative redshift of SSS17a. *LVC GCN Circ.* 21592 (2017).
37. D'Avanzo, P. et al. LIGO/Virgo G298048: ESO/VLT optical observations. *LVC GCN Circ.* 21653 (2017).
38. Grado, A. et al. LIGO/VIRGO G298048: INAF VST-ESO PARANAL observations. *LVC GCN Circ.* 21598 (2017).
39. Grado, A. et al. LIGO/VIRGO G298048: INAF VST-ESO PARANAL observations of NGC4993. *LVC GCN Circ.* 21703 (2017).
40. Bertin, E. & Arnouts, S. SExtractor: software for source extraction. *Astron. Astrophys. Suppl. Ser.* **117**, 393–404 (1996).
41. Capaccioli, M. & Schipani, P. The VLT survey telescope opens to the sky: history of a commissioning. *Messenger* **146**, 2–7 (2011).
42. Kuijken, K. OmegaCAM: ESO's newest imager. *Messenger* **146**, 8–11 (2011).
43. Grado, A., Capaccioli, M., Limatola, L. & Getman, F. VST processing facility: first astronomical applications. *Mem. Soc. Astron. It. Suppl.* **19**, 362 (2012).
44. Tody, D. IRAF in the Nineties. In *Astronomical Data Analysis Software and Systems II* (eds Hanisch, R. J. et al.) 173–183 (ASP Conf. Ser. Vol. 52, 1993).
45. Vernet, J. et al. X-shooter, the new wide band intermediate resolution spectrograph at the ESO Very Large Telescope. *Astron. Astrophys.* **536**, A105 (2011).
46. Freudling, W. et al. Automated data reduction workflows for astronomy. The ESO Reflex environment. *Astron. Astrophys.* **559**, A96 (2013).
47. Modigliani, A. et al. The X-shooter pipeline. *Proc. SPIE* **7737**, <http://dx.doi.org/10.1117/12.857211> (2010).
48. Moehler, S. et al. Flux calibration of medium-resolution spectra from 300 nm to 2500 nm: model reference spectra and telluric correction. *Astron. Astrophys.* **568**, A9 (2014).
49. Noll, S. et al. An atmospheric radiation model for Cerro Paranal. I. The optical spectral range. *Astron. Astrophys.* **543**, A92 (2012).
50. Jones, A. et al. An advanced scattered moonlight model for Cerro Paranal. *Astron. Astrophys.* **560**, A91 (2013).
51. Smette, A. et al. Molecfit: a general tool for telluric absorption correction. I. Method and application to ESO instruments. *Astron. Astrophys.* **576**, A77 (2015).
52. Kausch, W. et al. Molecfit: a general tool for telluric absorption correction. II. Quantitative evaluation on ESO-VLT/X-Shooter spectra. *Astron. Astrophys.* **576**, A78 (2015).
53. Horne, W. An optimal extraction algorithm for CCD spectroscopy. *Publ. Astron. Soc. Pac.* **98**, 609–617 (1986).
54. Fried, D. L. Limiting resolution looking down through the atmosphere. *J. Opt. Soc. Am.* **56**, 1380–1384 (1966).
55. Poznanski, D., Prochaska, J. X. & Bloom, J. S. An empirical relation between sodium absorption and dust extinction. *Mon. Not. R. Astron. Soc.* **426**, 1465–1474 (2012).
56. Munari, U. & Zwitter, T. Equivalent width of Na I and K I lines and reddening. *Astron. Astrophys.* **318**, 269–274 (1997).
57. Munari, U. et al. Diffuse interstellar bands in RAVE survey spectra. *Astron. Astrophys.* **488**, 969–973 (2008).
58. Schlafly, E. F. & Finkbeiner, D. P. Measuring reddening with Sloan Digital Sky Survey stellar spectra and recalibrating SFD. *Astrophys. J.* **737**, 103 (2011).
59. Harutyunyan, A. et al. ESC supernova spectroscopy of non-ESC targets. *Astron. Astrophys.* **488**, 383–399 (2008).
60. Mazzali, P., Valenti, S. & Della Valle, M. The metamorphosis of supernova SN 2008D/XRF 080109: a link between supernovae and GRBs/hypernovae. *Science* **321**, 1185–1188 (2008).
61. Levan, A. J. et al. LIGO/Virgo G298048: MUSE Integral Field Observations. *LVC GCN Circ.* 21681 (2017).
62. Hallinan, G. et al. A radio counterpart to a neutron star merger. *Science* <http://doi.org/10.1126/science.aap9855> (2017).
63. Cooke, et al., manuscript in preparation.
64. Alexander, K. D. et al. The electromagnetic counterpart of the binary neutron star merger LIGO/VIRGO GW170817. VI. Radio constraints on a relativistic jet and predictions for late-time emission from the kilonova ejecta. *Astrophys. J.* **848**, <https://doi.org/10.3847/2041-8213/aa905d> (2017).
65. Goldstein, A., Veres, P., von Kienlin, A., et al., LIGO/Virgo G298048 - update on Fermi/GBM GRB 170817A analysis. *LVC GCN Circ.* 21528 (2017).

66. D'Avanzo, P. et al. A complete sample of bright Swift short gamma-ray bursts. *Mon. Not. R. Astron. Soc.* **442**, 2342–2356 (2014).
67. Berger, E. Short-duration gamma-ray bursts. *Annu. Rev. Astron. Astrophys.* **52**, 43–105 (2014).
68. Ghisellini, G. et al. Are GRB980425 and GRB031203 real outliers or twins of GRB060218? *Mon. Not. R. Astron. Soc.* **372**, 1699–1709 (2006).
69. Salafia, O. S., Ghisellini, G., Pescalli, A., Ghirlanda, G. & Nappo, F. Light curves and spectra from off-axis gamma-ray bursts. *Mon. Not. R. Astron. Soc.* **461**, 3607–3619 (2016).
70. Wanderman, D. & Piran, T. The rate, luminosity function and time delay of non-Collapsar short GRBs. *Mon. Not. R. Astron. Soc.* **448**, 3026–3037 (2015).
71. Ghirlanda, G. et al. Short gamma-ray bursts at the dawn of the gravitational wave era. *Astron. Astrophys.* **594**, A84 (2016).
72. Fong, W. et al. The afterglow and early-type host galaxy of the short GRB 150101B at $z = 0.1343$. *Astrophys. J.* **833**, 151 (2016).
73. Ghirlanda, G. et al. Gamma-ray bursts in the comoving frame. *Mon. Not. R. Astron. Soc.* **420**, 483–494 (2012).
74. Liang, E.-W. et al. A comprehensive study of gamma-ray burst optical emission. II. Afterglow onset and late re-brightening components. *Astrophys. J.* **774**, 13 (2013).
75. Haggard, D. et al. A deep chandra X-ray study of neutron star coalescence GW170817. *Astrophys. J.* **848**, <https://doi.org/10.3847/2041-8213/aa8ede> (2017).
76. Moldon, J. & Beswick, R. LIGO/Virgo G298048: e-MERLIN upper limits on 5 GHz compact emission from SSS17a. *LVC GCN Circ.* 21804 (2017).
77. Mooley, K. et al. LIGO/VIRGO G298048: MeerKAT observations of SSS17a. *LVC GCN Circ.* 21891 (2017).
78. van Eerten, H. J., Leventis, K., Meliani, Z., Wijers, R. A. M. J. & Keppens, R. Gamma-ray burst afterglows from transrelativistic blast wave simulations. *Mon. Not. R. Astron. Soc.* **403**, 300–316 (2010).

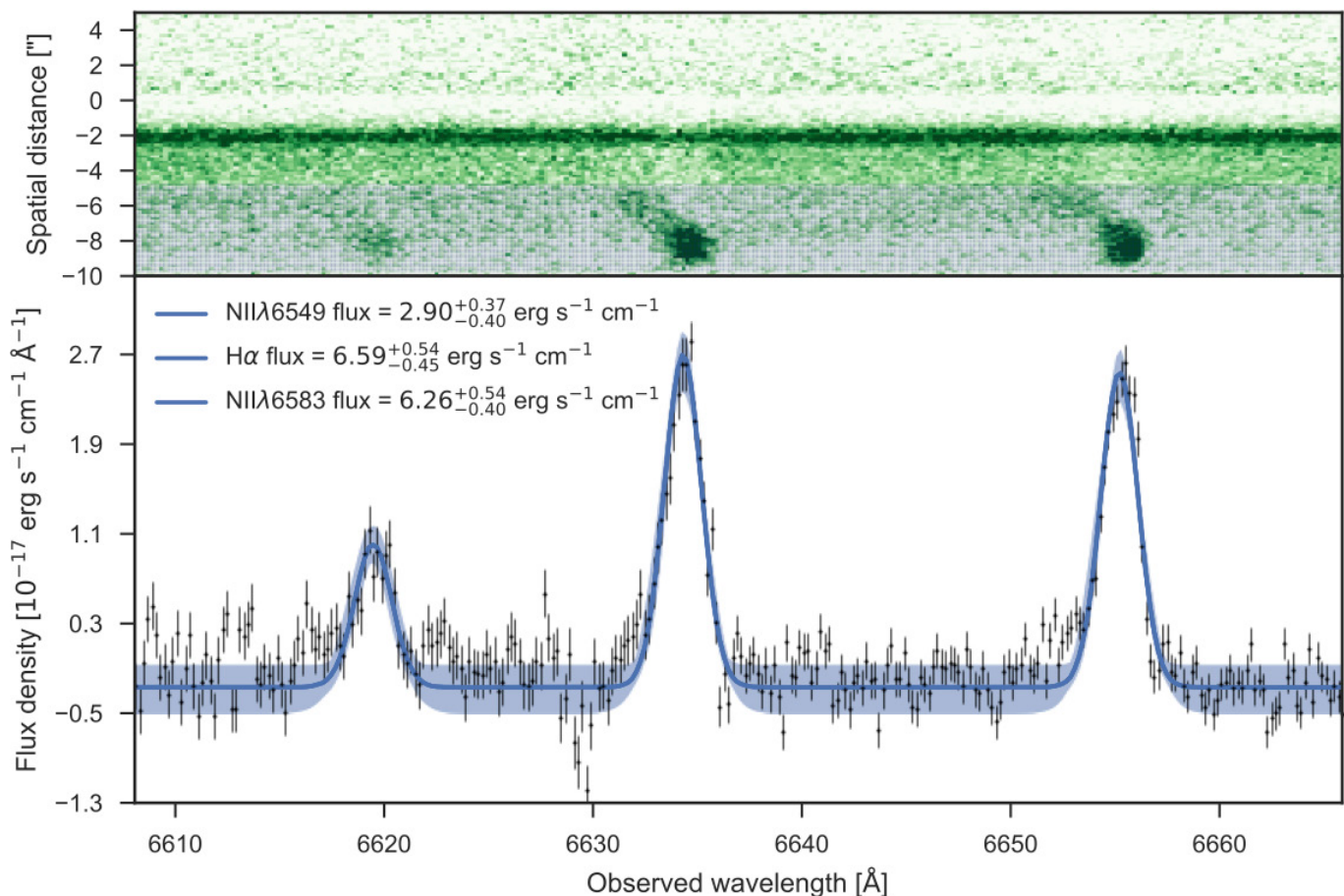


Extended Data Figure 1 | Image of the NGC 4993 galaxy. The image was obtained with the X-shooter acquisition camera (z filter). The X-shooter slit overlaid in red. The position of the OT has been marked by a blue circle. The position of the line emission in the slit has been also marked. The dust lanes visible in the host intersect the slit at the position of the line emission.



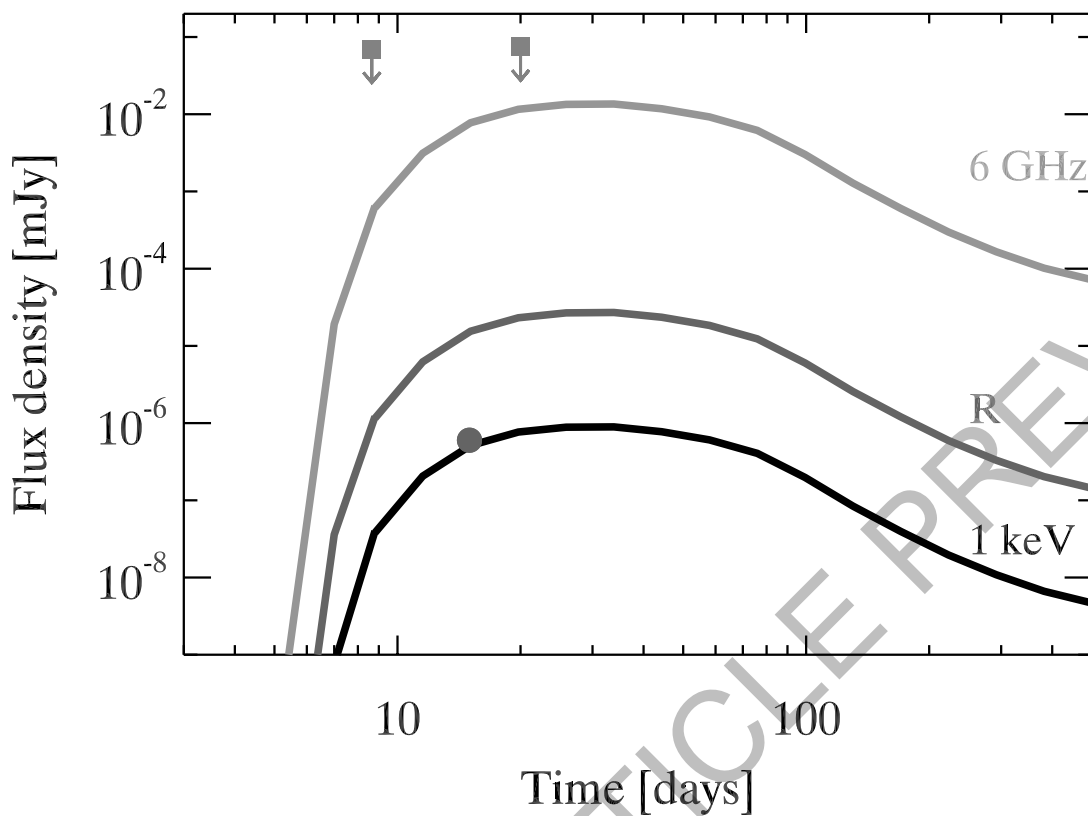
Extended Data Figure 2 | Black-body fit to the SSS17a/DLT17ck spectra. The two early X-shooter spectra of GW170817, obtained 1.5 d and 3.5 d after discovery are compared with the spectra of the type Ib SN 2008D⁶⁰

obtained at 2–5 days after explosion respectively (blue, arbitrarily scaled in flux). The dotted line show the black-body fit of the optical continuum of GW170817 with temperature 5,000 K and 3,200 K, respectively.



Extended Data Figure 3 | 2D image of the SSS17a/DLT17ck spectrum. The upper panel shows the rectified, X-shooter 2D-image. The dark line visible across the entire spectral window is the bright continuum of the OT and the offset, dark blobs indicate the position of the line emission from

N II λ6,549, Hα, and N II λ6,583. The lower panel shows an extraction of the line emission where the line fits are overlain. The integrated line fluxes are given in the labels, normalized by a factor of 10^{-17} for clarity.



Extended Data Figure 4 | Off-axis GRB afterglow modeling. Synthetic X-ray, optical and radio light curve of the GRB afterglow as predicted in an off-axis jet model. The filled dot symbol shows the X-ray detection (ref. 23) and the arrows two representative radio upper limits^{76,77}

Extended Data Table 1 | Log of photometric observations

MJD ^a	Phase ^b (days)	Telescope	Instrument	Exposure (seconds)	Filter	Mag ^c
57987.02	4.5	VLT	FORS2	480	B	22.729 ± 0.128
57989.02	6.5	VLT	FORS2	600	B	23.807 ± 0.251
57991.01	8.5	VLT	FORS2	600	B	24.581 ± 0.363
57983.05	0.5	REM	ROS2	720	g	17.320 ± 0.070
57984.00	1.5	VLT	XS	90	g	18.553 ± 0.060
57984.03	1.5	REM	ROS2	720	g	18.591 ± 0.068
57984.96	2.5	REM	ROS2	720	g	20.314 ± 0.282
57986.02	3.5	VLT	XS	90	g	20.940 ± 0.060
57987.99	5.5	VST	OmegaCam	200	g	22.507 ± 0.122
57988.02	5.5	VLT		90	g	22.332 ± 0.100
57987.02	4.5	VLT	FORS2	240	V	21.082 ± 0.054
57989.02	6.5	VLT	FORS2	600	V	22.361 ± 0.158
57991.01	8.5	VLT	FORS2	600	V	23.152 ± 0.256
57993.01	10.5	VLT	FORS2	840	V	23.761 ± 0.280
57983.05	0.5	REM	ROS2	720	r	17.140 ± 0.080
57983.98	1.5	REM	ROS2	720	r	17.675 ± 0.134
57984.00	1.5	VLT	XS	90	r	17.951 ± 0.020
57984.96	2.5	REM	ROS2	720	r	19.178 ± 0.100
57986.02	3.5	VLT	XS	90	r	19.740 ± 0.020
57986.97	4.5	VLT	FORS2	240	R	20.238 ± 0.058
57988.02	5.5	VLT	XS	90	r	20.740 ± 0.030
57988.98	6.5	VST	OmegaCam	200	r	21.310 ± 0.075
57989.00	6.5	VLT	FORS2	240	R	21.268 ± 0.106
57991.00	8.5	VLT	FORS2	240	R	22.501 ± 0.240
57993.01	10.5	VLT	FORS2	360	R	23.379 ± 0.277
57983.05	0.5	REM	ROS2	720	i	16.984 ± 0.050
57983.98	1.5	REM	ROS2	720	i	17.664 ± 0.064
57984.96	2.5	REM	ROS2	720	i	18.354 ± 0.105
57987.01	4.5	VLT	FORS2	300	I	19.284 ± 0.055
57988.97	6.5	VST	OmegaCam	200	i	20.329 ± 0.089
57988.98	6.5	VLT	FORS2	300	I	20.142 ± 0.072
57990.99	8.5	VLT	FORS2	300	I	21.133 ± 0.119
57992.99	10.5	VLT	FORS2	300	I	22.052 ± 0.289
57994.00	11.5	VLT	FORS2	630	I	23.000 ± 0.309
57983.05	0.5	REM	ROS2	720	z	16.854 ± 0.100
57983.98	1.5	REM	ROS2	720	z	17.611 ± 0.098
57984.00	1.5	VLT	XS	90	z	17.654 ± 0.070
57986.02	3.5	VLT	XS	90	z	18.300 ± 0.020
57987.00	4.5	VLT	FORS2	300	z	18.927 ± 0.027
57988.02	5.5	VLT	XS	90	z	19.160 ± 0.030
57988.98	6.5	VLT	FORS2	300	z	19.627 ± 0.039
57990.99	8.5	VLT	FORS2	300	z	20.606 ± 0.092
57992.98	10.5	VLT	FORS2	600	z	22.014 ± 0.214
57993.98	11.5	VLT	FORS2	720	z	22.815 ± 0.471
57996.98	14.5	VLT	FORS2	1350	z	23.342 ± 0.368

^aJD – 2,400,000.5.^bAfter GW trigger time.^cAB magnitudes, not corrected for Galactic extinction ($E_{B-V}=0.11$).

Extended Data Table 2 | Log of spectroscopic observations

UT ^a	MJD ^b	Phase ^c (days)	Instrument	Slit/Grism (arcsec)	Exp.Time (s)	Airmass (min/max)	Seeing (arcsec)	F ^d _{Vis}	F ^d _{NIR}
18.97	57983.97	1.5	VLT/X-shooter	1.0/0.9/0.9	2400	1.45/1.72	0.61	166	40
19.95	57984.95	2.5	Gemini-S/GMOS	—	600	2.5/2.7	—	53	—
20.98	57985.98	3.5	VLT/X-shooter	1.0/0.9/0.9	3600	1.52/2.12	0.9	27.8	36.5
21.98	57986.98	4.5	VLT/FORS2	600RI	1800	1.58/1.86	0.88	18	—
22.03	57987.03	4.5	VLT/FORS2	600B	700	2.60/2.91	0.59	18	—
22.98	57987.98	5.5	VLT/X-shooter	1.0/0.9/0.9	3600	1.58/2.25	0.71	10.8	23.9
23.98	57988.98	6.5	VLT/X-shooter	1.0/0.9/0.9	3600	1.74/2.33	0.87	7.0	15.4
24.98	57989.98	7.5	VLT/X-shooter	1.0/0.9/0.9	3600	1.66/2.44	0.53	6.3	12
25.98	57990.98	8.5	VLT/X-shooter	1.0/0.9/0.9	2400	1.74/1.98	0.65	6.1	8.2
26.97	57991.97	9.5	VLT/X-shooter	1.0/0.9/0.9	3600	1.69/2.50	0.78	5.1	6.0
27.97	57992.97	10.5	VLT/X-shooter	1.0/0.9/0.9	3600	1.70/2.53	0.67	4.7	4.5

^aUT days of August 2017.^bJD – 2,400,000.5.^cAfter GW trigger time.^dFluxes at 6,000 Å and 15,000 Å in 10^{-18} erg s⁻¹ cm⁻² Å⁻¹, not corrected for reddening; uncertainties are about 10%.